Article

Design Optimization of an Enhanced-Mode GaN HEMT with Hybrid Back Barrier and Breakdown Voltage Prediction Based on Neural Networks

Kuiyuan Tian, Jinwei Hu, Jiangfeng Du *[ID] and Qi Yu

State Key Laboratory of Electronic Thin Films and Integrated Devices, University of Electronic Science and Technology of China, Chengdu 610054, China; tky@std.uestc.edu.cn (K.T.); jinweihu@std.uestc.edu.cn (J.H.); qiyu@uestc.edu.cn (Q.Y.)
* Correspondence: jfdu@uestc.edu.cn

Abstract: To improve the breakdown voltage (BV), a GaN-based high-electron-mobility transistor with a hybrid AlGaN back barrier (HBB-HEMT) was proposed. The hybrid AlGaN back barrier was constructed using the $Al_{0.25}Ga_{0.75}N$ region and $Al_{0.1}G_{0}.9N$ region, each with a distinct Al composition. Simulation results of the HBB-HEMT demonstrated a breakdown voltage (1640 V) that was 212% higher than that of the conventional HEMT (Conv-HEMT) and a low on-resistance (0.4 mΩ·cm^2). Ultimately, the device achieved a high Baliga's figure of merit (7.3 GW/cm^2) among reported devices of similar size. A back-propagation (BP) neural network-based prediction model was trained to predict BV for enhanced efficiency in subsequent work. The model was trained and calibrated, achieving a correlation coefficient (R) of 0.99 and a prediction accuracy of 95% on the test set. The results indicated that the BP neural network model using the Levenberg–Marquardt algorithm accurately predicted the forward breakdown voltage of the HBB-HEMT, underscoring the feasibility and significance of neural network models in designing GaN power devices.

Keywords: GaN HEMT; hybrid AlGaN back barrier; breakdown voltage; BP neural networks; value prediction

1. Introduction

Gallium nitride high-electron-mobility transistors (GaN HEMTs) have a wide range of applications in power and RF electronics due to the favorable characteristics of high switching speed, high electron mobility, wide bandgap, and thermal stability [1–6]. It is necessary to design normally-off GaN HEMTs to increase safety and reliability in circuit design [7,8]. Several techniques have been reported to realize normally-off GaN HEMTs, including cascode structures [9], recessed gates [10,11], fluorine ion implantation [12], ultra-thin barrier layers [13], and p-(Al)GaN cap layers [14–18]. Among these techniques, the p-GaN cap layer structure stands out for its widespread adoption in commercial applications, attributed to its straightforward design, robustness, and superior performance. However, these devices have only achieved an average breakdown electric field of 1.4 MV/cm and Baliga's figure of merit (FOM) of 3.9 GW/cm^2, respectively [17]. These figures are still significantly less than the critical breakdown electric field of 3 MV/cm.

The electric field distribution of the channel in a GaN HEMT is non-uniform during breakdown, with the electric field concentrating at the gate edges. This causes breakdown to occur first at the gate edges, which results in a lower average breakdown field. In addition, defects in the GaN material and interface states introduced during the fabrication process can lead to local electric field enhancement, further reducing the actual breakdown field of the device. Gate field plates or drain field plates are usually introduced to alleviate the local electric field enhancement problem [2]. However, the field plate structure introduces additional parasitic capacitance, which degrades the high-frequency characteristics of GaN

HEMT devices [19]. GaN HEMTs with a back-barrier structure [20] can relieve electric field crowding without sacrificing high-frequency characteristics, but the balance between on-resistance ($R_{on, sp}$) and breakdown voltage (BV) is still not good enough.

Moreover, the BV of a GaN HEMT normally depends on multiple parameters such as barrier layer thickness, gate-to-drain distance, and specific parameters in special structures. These parameters are intricately coupled due to complex physical mechanisms within the GaN HEMT. Consequently, using simulation and experimental testing methods to continuously approach the target value requires significant time investment, leading to long optimization cycles and low efficiency in device design. The rise of the backpropagation neural network algorithm (BP) provides a more efficient solution for device design optimization. This algorithm employs a multidimensional nonlinear approximator to map input parameters to output parameters and possesses strong self-learning capabilities, making it particularly suitable for addressing the complex physical mechanisms within GaN HEMTs. Although there have been some studies reporting the use of neural networks for performance prediction in device design [21–24], there has been little research on the performance optimization of GaN HEMTs.

In this paper, a GaN-based high-electron-mobility transistor with a hybrid AlGaN back barrier (HBB-HEMT) is proposed to improve breakdown performance. The proposed HBB-HEMT was simulated with the Silvaco TCAD. Before the actual simulation, the simulation models [25–30] were calibrated by comparison with the experimental results [31], thus proving the correctness of the models. Based on simulation tools, the DC, breakdown, and CV characteristics of the HBB-HEMT were discussed and optimized. The final optimized results demonstrate that the HBB-HEMT has low $R_{on, sp}$, high BV, and high FOM, which shows significant potential in electronic power applications. Finally, L_{gd} (gate-to-drain distance), L_{gi} (gate-to-$Al_{0.25}Ga_{0.75}N/Al_{0.1}Ga_{0.9}N$ interface distance), and T_{buf} (thickness of the GaN buffer) were selected as the neural network model inputs, while the breakdown voltage was designated as the output. The neural network model was trained using data obtained from TCAD simulations. The resulting predictions showed a low error rate compared to the simulation values, demonstrating the accuracy of the model.

2. Device Structure

The structure of the conventional p-GaN gate GaN HEMT (Conv HEMT) is shown in Figure 1a. The structures of the p-GaN gate GaN HEMT with a single AlGaN back barrier (B-HEMT) are depicted in Figure 1b,c, with the aluminum composition (Al.comp) of the AlGaN back barrier set to 0.1 and 0.25, respectively. Figure 1d illustrates the proposed HBB-HEMT, in which the hybrid AlGaN back barrier consists of an $Al_{0.25}Ga_{0.75}N$ region and an $Al_{0.1}Ga_{0.9}N$ region, and the $Al_{0.25}Ga_{0.75}N/Al_{0.1}Ga_{0.9}N$ interface is set between the gate and the drain. The above four structures consist of a Si(111) substrate, GaN buffer layer, GaN channel layer, $Al_{0.26}Ga_{0.74}N$ barrier layer, and p-GaN layer doped with 3×10^{17} cm^{-3}. Table 1 provides the key structural parameters for the HBB-HEMT. For the HBB-HEMT, the $Al_{0.25}Ga_{0.75}N/Al_{0.1}Ga_{0.9}N$ interface location (L_{gi}), the thickness of GaN buffer (T_{buf}), and gate-to-drain distance (L_{gd}) have been optimized.

Table 1. Key parameters of HBB-HEMT.

Parameter	Unit	Value	Parameter Caption
L_g	μm	1.4	Length of the gate region
L_{gi}	μm	1–6	Gate to the interface distance
L_{gs}	μm	1	Distance from gate to source
L_{gd}	μm	5~20	Distance from gate to drain
$T_{P\text{-}GaN}$	nm	110	Thickness of p-GaN layer
T_{bar}	nm	15	Thickness of AlGaN barrier layer
T_{ch}	nm	35	Thickness of GaN channel layer
T_{buf}	μm	0.1~4	Thickness of GaN buffer layer
T_{bb}	nm	50	Thickness of AlGaN back barrier layer
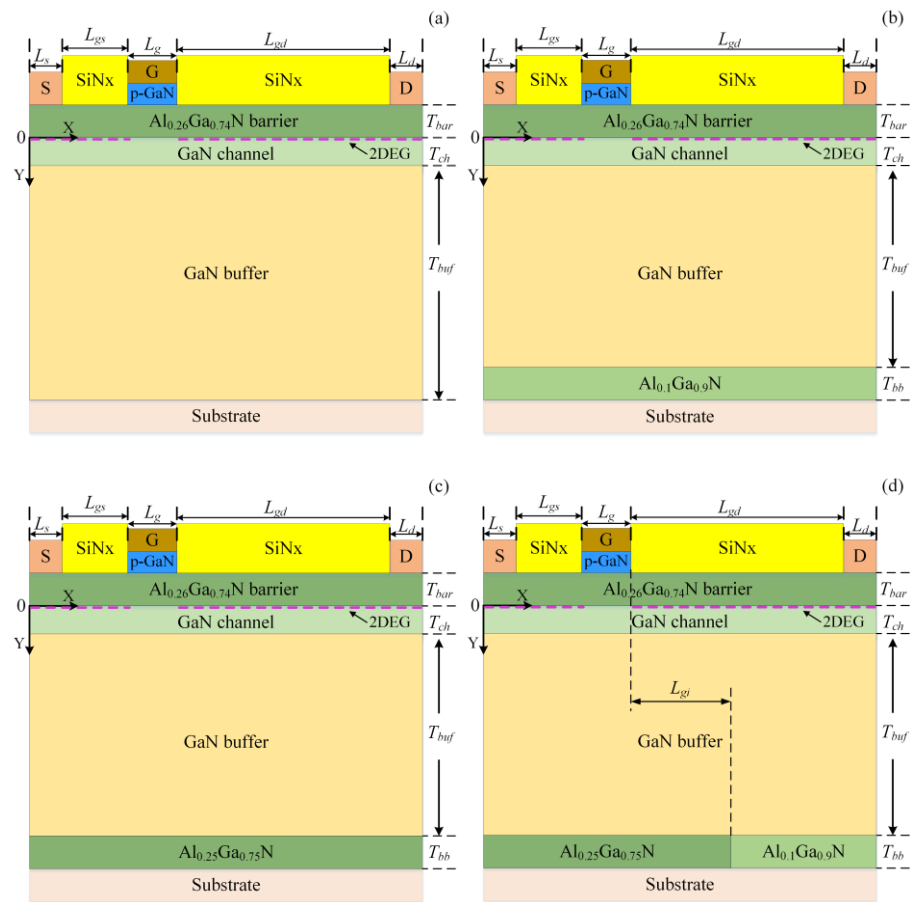
Figure 1. Schematic cross section of the (**a**) Conv HEMT, (**b**) B-HEMT (Al.comp = 0.1), (**c**) B-HEMT (Al.comp = 0.25), and (**d**) HBB-HEMT.

3. Simulation Models

3.1. Simulation Models

In the simulation, various models were utilized, including the GaN polarization model, the mobility model, and the impact ionization model. The characteristics of the 2D electron gas are explained through the GaN polarization model. In the GaN polarization model, the total polarization (P_t) consists of spontaneous polarization (P_{sp}) and piezoelectric polarization (P_{pe}). Therefore, the P_t of GaN or $Al_xGa_{1-x}N$ is [25]:

$$P_t = P_{sp} + P_{pe} \tag{1}$$

For $Al_xGa_{1-x}N$, the spontaneous polarization intensity P_{sp} is given by [26]:

$$P_{sp}(Al_xGa_{1-x}N) = xP_{sp}(AlN) + (1-x)P_{sp}(GaN) \tag{2}$$

In this context, the value for $P_{sp}(AlN)$ is -0.09 and the value for $P_{sp}(GaN)$ is -0.034. The piezoelectric polarization intensity P_{pe} is described as [27]:

$$P_{pe}(Al_xGa_{1-x}N) = 2\varepsilon(Al_xGa_{1-x}N)\left(e_{31} - e_{33}\frac{C_{13}}{C_{33}}\right) \tag{3}$$

Let $a(Al_xGa_{1-x}N)$ be the lattice constant of AlGaN. The strain $\varepsilon(Al_xGa_{1-x}N)$ in AlGaN is described as follows:

$$\varepsilon(Al_xGa_{1-x}N) = \frac{a_{GaN} - a(Al_xGa_{1-x}N)}{a(Al_xGa_{1-x}N)} \tag{4}$$

$$a(Al_xGa_{1-x}N) = (1 - x)a_{GaN} + xa_{AlN} \tag{5}$$

in which C_{13} and C_{33} represent elastic constants, e_{31} and e_{33} are piezoelectric constants of GaN, and a_{GaN} and a_{AlN} are the lattice constants of GaN and AlN, respectively. During the simulation, e_{31}, e_{33}, C_{13}, C_{33}, a_{GaN}, and a_{AlN} were set to -0.34, 0.67, 100, 392, 3.189, and 3.112, respectively. From the above formula, the strain $\varepsilon(Al_xGa_{1-x}N)$ in AlGaN increases with Al composition. As the strain $\varepsilon(Al_xGa_{1-x}N)$ increases, the piezoelectric polarization $P_{pe}(Al_xGa_{1-x}N)$ in AlGaN also enhances. In this study, the Al composition was 0.26, and the tensile strain in AlGaN was approximately 0.63%.

In this study, the current characteristic of p-GaN HEMTs was described using the mobility model. During the simulation, the Albrecht model was chosen as the low-field mobility model, which was described as a function of doping concentration N and lattice temperature T [28]:

$$\frac{1}{\mu(N,T)} = \frac{a \cdot N}{N_0} \left(\frac{T}{T_0}\right)^{-3/2} \ln\left(1 + 3\left(\frac{T}{T_0}\right)^2 \left(\frac{N}{N_0}\right)^{-2/3}\right) + b\left(\frac{T}{T_0}\right)^{3/2} + \frac{c}{\exp(T_1/T_L) - 1}, \tag{6}$$

In expression (6), a, b, c, N_0, T_0, and T_1 are set to 2.61×10^{-4} V·s·cm^{-2}, 2.9×10^{-4} V·s·cm^{-2}, 170.0×10^{-4} V·s·cm^{-2}, 1.0×10^{17} cm^{-3}, 300 K, and 1065 K.

The high-field mobility $\mu(E)$ depends on the electric field E [29]:

$$\mu(E) = \frac{\mu(N, T) + V_{sat} \frac{E^{n1-1}}{E_c^{n1}}}{1 + \alpha\left(\frac{E}{E_c}\right)^{n2} + \left(\frac{E}{E_c}\right)^{n1}} \tag{7}$$

In this context, $\mu(N, T)$ is the low-field mobility in Equation (7). For Equation (7), V_{sat}, E_c, α, n1, and n2 are set to 1.9064×107 cm/s, 220.8936 kV/cm, 6.1973, 7.2044, and 0.7857, respectively.

In this study, the Selberherr impact ionization model was used to simulate the breakdown characteristic. In the model, the impact ionization rates for holes (α_p) and electrons (α_n) are described as [30]:

$$\alpha_n = a_n \exp\left[-\left(\frac{b_n}{E}\right)^m\right] \tag{8}$$

$$\alpha_p = a_p \exp\left[-\left(\frac{b_p}{E}\right)^m\right] \tag{9}$$

In Equations (8) and (9), the impact ionization rates of holes (α_p) and electrons (α_n) depend on the local electric field. According to the experimental results, the parameters at room temperature were set as follows: m = 1.1438×10^7 cm^{-1}, a_n = 1.1438×10^7 cm^{-1}, a_p = 23.8933 MV/cm, b_n = 23.8933 MV/cm, and b_p = 13.2.

3.2. Simulation Calibration

We fabricated a D-mode GaN HEMT to fit the simulation model [31]. The epitaxial structures with a dislocation density of 10^9 cm^{-2} were grown on Si substrates. The epitaxial structures consisted of a 4 nm thick GaN cap layer, a 21 nm thick AlGaN barrier layer, and a 3.2 μm thick GaN buffer layer. First, a 20 nm thick SiN$_x$ was grown as the gate dielectric by low-pressure chemical vapor deposition (LPCVD), which was selectively etched into the gate pattern by inductively coupled plasma etching (ICP-RIE) using SF$_6$ mixed gas. Then, sputtered Ni/Au was deposited on the gate dielectric SiN$_x$ as the gate electrode. The Ti/Al/Ni/Au stack was deposited and rapidly annealed at 870 °C to form the source and drain ohmic contacts. A 150 nm thick SiN$_x$ was formed on the GaN cap layer for passivation and argon ion implantation for isolation. The gate width, gate length, gate-to-source distance, and gate-to-drain distance of the fabricated transistor were 250 μm, 2 μm, 2 μm, and 2 μm, respectively. The structural parameters used in the simulation

were the same as those in the experiment. The fabricated D-mode GaN HEMT was tested by the Agilent B1505 and its test data were used to fit the models described above. The simulated threshold voltage (V_{th}) of GaN HEMT was −7.8 V, which is consistent with the experiment. Figure 2 presents the simulated output characteristics and the fabricated GaN HEMT output characteristics. The results demonstrate a good fitting, which proves the reliability of the simulation models for GaN HEMTs.
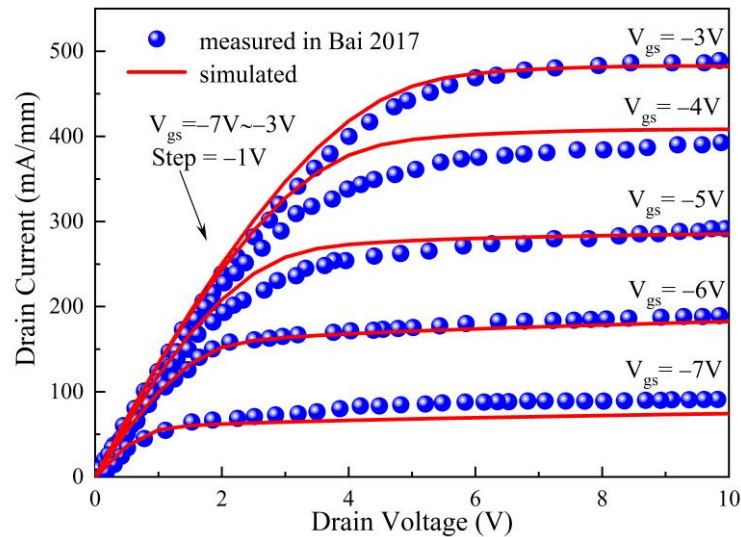

Figure 2. Comparison of measured and simulated values of the GaN HEMT output characteristics by calibrating the simulation models [31].

4. Results and Discussions

4.1. DC Properties

Figure 3a displays the transfer curves of the Conv HEMT, B-HEMTs, and HBB-HEMT. The simulation indicates that the V_{th} of the four devices is 1 V. Figure 3b shows that the saturation current of the four devices is 0.9 A/mm, and the on-resistance ($R_{on, sp}$) is 0.4 mΩ·cm^2 when the gate-source voltage V_{gs} is 4 V. Compared with Conv HEMT, the AlGaN back barrier does not affect the transfer and output characteristics of HEMT, which improves breakdown characteristics without sacrificing DC characteristics.
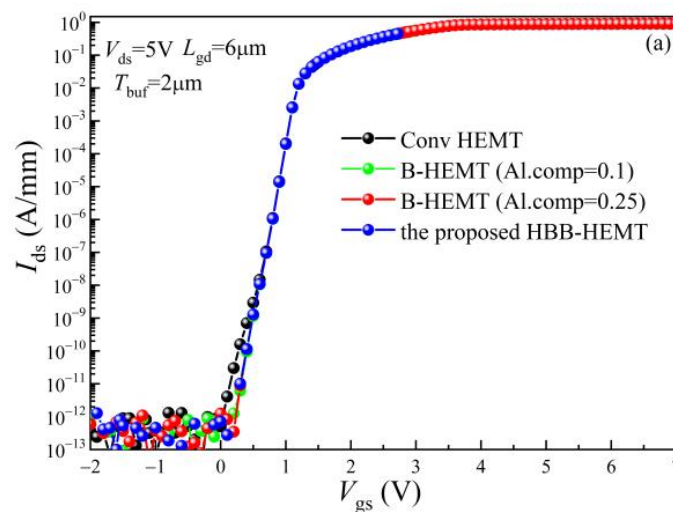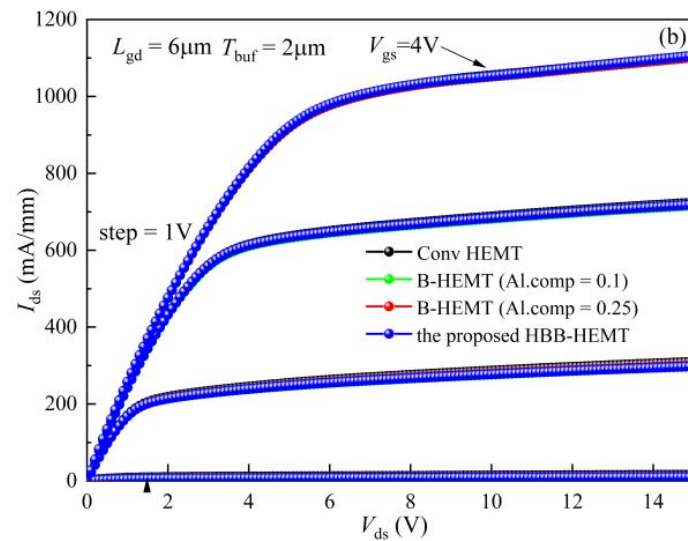

Figure 3. *Cont.*

Figure 3. (**a**) Transfer performances and (**b**) output performances for the HEMTs.

4.2. Breakdown Properties

The breakdown characteristics of four GaN HEMT devices were simulated. Figure 4 presents the contour plot of the electric field distribution during device breakdown. Electric field concentration occurs on the gate side in the buffer layers of Conv HEMT and B-HEMT (Al.comp = 0.1). Then, the electric field diminishes rapidly with increasing distance from the gate. However, the electric field displays a more uniform distribution for B-HEMT with an Al.comp of 0.25. Two-dimensional hole gas (2DHG) is formed at the interface between the GaN buffer layer and the AlGaN back-barrier layer due to piezoelectric polarization. The 2DHG generates an upward vertical electric field in the channel, which counteracts the downward vertical electric field caused by the positive polarization charges in the barrier layer. Consequently, by reducing the local electric field enhancement effect, the electric field distribution in the channel is more uniform. As the Al composition in the back-barrier increases, the concentration of the 2DEG also increases, which enhances the upward vertical electric field. Therefore, the electric field distribution in B-HEMT (Al.comp = 0.25) is more uniform than that in B-HEMT (Al.comp = 0.1) by further weakening the downward vertical electric field within the channel.
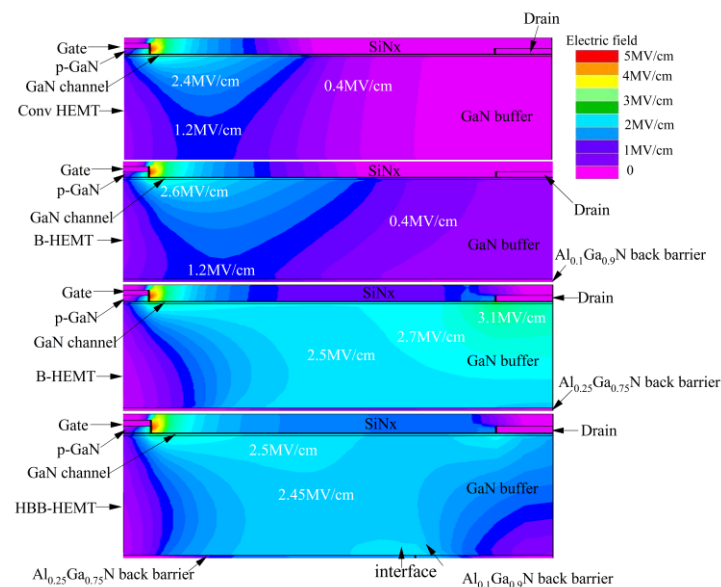

Figure 4. Electric field distribution contours for the GaN HEMT devices under breakdown conditions.

However, another electric field crowding region will occur near the drain electrode of B-HEMT (Al.comp = 0.25), which leads to early breakdown near the drain electrode. For the proposed HBB-HEMT, due to the modulation of the electric field by the hybrid AlGaN back-barrier structure, the electric field at the drain side is reduced, resulting in a more uniform electric field distribution across the buffer layer, channel, and passivation layer. The electric field reaches 3 MV/cm in the center of the buffer layer. The electric field modulation of the buffer layer in the hybrid AlGaN back-barrier structure primarily arises from the variance in relative permittivity between the $Al_{0.25}Ga_{0.75}N$ and $Al_{0.1}Ga_{0.9}N$ zones. The relative permittivity of $Al_xGa_{1-x}N$ (where $0 \leq x \leq 1$) can be computed using the following formula:

$$\varepsilon(Al_xGa_{1-x}N) = 8.5x + 8.9(1-x) \tag{10}$$

The discrepancy in relative permittivity between the $Al_{0.25}Ga_{0.75}N$ and $Al_{0.1}Ga_{0.9}N$ zones stems from the distinct Al compositions, with relative permittivities of 8.5 and 8.9 for AlN and GaN, respectively. This variation in Al content influences the relative permittivity. Based on Gauss's law, the electric fields of the $Al_{0.25}Ga_{0.75}N$ zone (E_1) and the $Al_{0.1}Ga_{0.9}N$ zone (E_2) are related as follows:

$$\varepsilon_1 E_1 = \varepsilon_2 E_2 \tag{11}$$

The discrepancy in relative permittivity between the $Al_{0.25}Ga_{0.75}N$ and $Al_{0.1}Ga_{0.9}N$ zones is denoted by ε_1 and ε_2, respectively. This variance results in an electrical field discontinuity along the $Al_{0.25}Ga_{0.75}N/Al_{0.1}Ga_{0.9}N$ interface. Such a discontinuity in the electrical field can then alter the electric field distributions between the gate and drain.

Figure 5a illustrates the one-dimensional electric field distribution in the channel of four devices when breakdown occurs. Electric field crowding occurs in the Conv HEMT and B-HEMTs. For Conv HEMT and B-HEMT (Al.comp = 0.1), the electric field peak is on the gate side. For B-HEMT (Al.comp = 0.25), another peak appears on the drain side, which is consistent with the results reported previously [18]. Figure 5b displays the breakdown curves of four GaN HEMTs, where V_{gs} is set to -3 V during the breakdown simulation. The BV of Conv HEMT is identified as 525 V, which is similar to the reported result of 510 V with similar dimensions [32]. The breakdown voltages are determined as follows: 615 V for B-HEMT (Al composition = 0.1), 940 V for B-HEMT (Al composition = 0.25), and 1225 V for the proposed HBB-HEMT, with BV defined as V_{ds} at $I_{ds} = 1$ μA/mm.
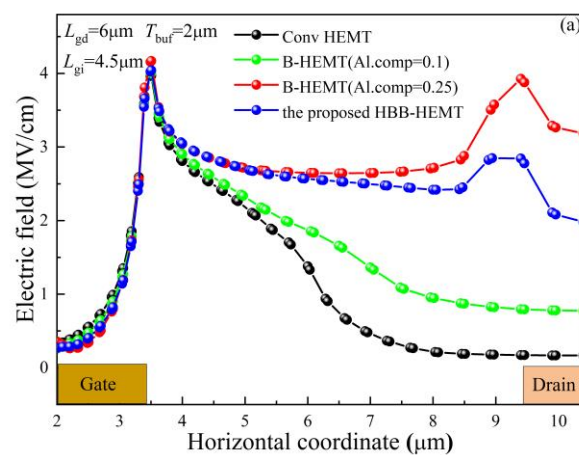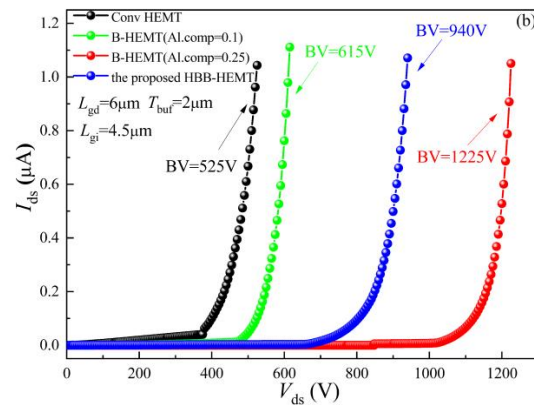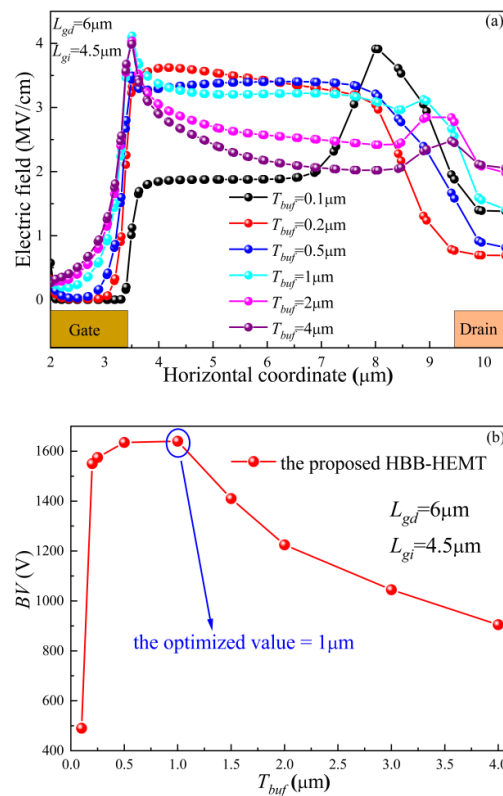

Figure 5. *Cont.*

Figure 5. (**a**) One-dimensional distribution of electric field along the GaN channel and (**b**) breakdown characteristics of GaN HEMTs.

To improve the modulation ability of the hybrid AlGaN back barrier of the proposed HBB-HEMT, the thickness of the GaN buffer layer is optimized. Figure 6a illustrates the channel electric field distribution of the HBB-HEMT under breakdown conditions with different T_{buf} values. When T_{buf} is reduced to a minimal value (0.1 μm), the electric field peak on the gate side is eliminated, and a new electric field peak appears at the $Al_{0.25}Ga_{0.75}N/Al_{0.1}Ga_{0.9}N$ interface. With the increase of T_{buf}, the electric field peak gathered on the drain side is reduced. However, when T_{buf} is larger than 1 μm, the electric field crowding near the gate increases. Therefore, when the GaN buffer thickness exceeds a certain threshold (1 μm), the modulation ability of the hybrid AlGaN back barrier decreases. Figure 6b shows the simulated BV of the HBB-HEMT with different T_{buf} values. Consistent with the results shown in Figure 6a, the highest BV (1640 V) is obtained when T_{buf} is 1 μm. Therefore, the optimized value of T_{buf} is determined to be 1 μm.

Figure 6. (**a**) One-dimensional distribution of electric field along the GaN channel and (**b**) breakdown voltage of GaN HBB-HEMTs vary with T_{buf}.

To further improve the withstand voltage capability of the HBB-HEMT, we optimized the position of the $Al_{0.25}Ga_{0.75}N$ / $Al_{0.1}Ga_{0.9}N$ interface. Figure 7a shows the distribution of the electric field in the channel for different L_{gi} values under breakdown conditions. For a given L_{gd} value, the electric field near the drain will decrease with a minuscule L_{gi} value, resulting in the overall average breakdown electric field in the channel far below the limit of the GaN. When the L_{gi} value is large, an electric field peak on the drain edge causes early breakdown, similar to what is seen in B-HEMT (Al.comp = 0.25) in Figure 5a. Figure 7b depicts the simulated breakdown voltage curves of HBB-HEMT with different L_{gi} values. As illustrated in Figure 7b, the breakdown voltage initially increases and then decreases as L_{gi} increases. The highest BV of 1640 V is achieved at L_{gi} = 4.5 μm.
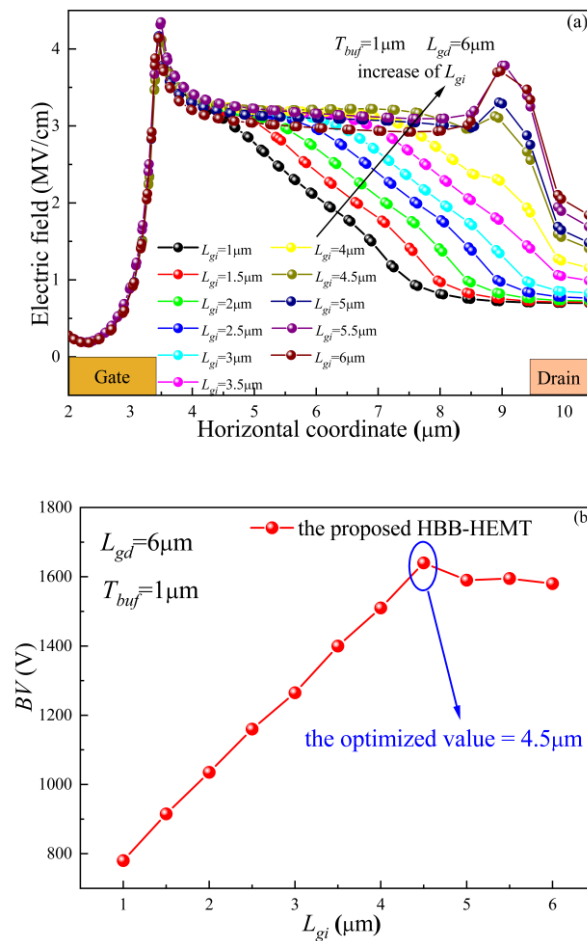
Figure 7. (**a**) One-dimensional distribution of electric field along the GaN channel under breakdown conditions and (**b**) breakdown voltage of GaN HBB-HEMT devices as a function of L_{gi}.

Figure 8 illustrates the breakdown voltages, $R_{on, sp}$, and FOM of the HBB-HEMTs with different L_{gd} values, and for each device, the value of L_{gi} is set as L_{gd}-1.5 μm. Consistent with the GaN HEMTs reported in [17], the BV of the proposed HBB-HEMT increases with increasing L_{gd}. When L_{gd} is increased from 5 μm to 20 μm, BV is increased from 1350 V to as high as 4180 V. Compared to the results reported in [21], the proposed HBB-HEMT with the same L_{gd} exhibits a higher BV. Increasing L_{gd} can lead to a higher BV for HBB-HEMT, but also results in a higher specific on-resistance. When L_{gd} is increased to 20 μm, $R_{on, sp}$ linearly increases to 2.2 mΩ·cm². Figure 8 also shows the calculated FOM for the proposed HBB-HEMT devices with different L_{gd} values. When L_{gd} is set to 10 μm, the highest FOM achieved is up to 9.3 GW/cm². When L_{gd} is set between 5 μm and 20 μm, the average breakdown electric field is larger than 2.6 MV/cm, and the highest average breakdown electric field (2.74 MV/cm) is obtained with a L_{gd} of 7 μm, which is very close to the GaN

limit (3 MV/cm). The results indicate that the HBB-HEMT possesses high breakdown voltage with a large L_{gd} when the location of the $Al_{0.25}Ga_{0.75}N/Al_{0.1}Ga_{0.9}N$ interface is properly designed.
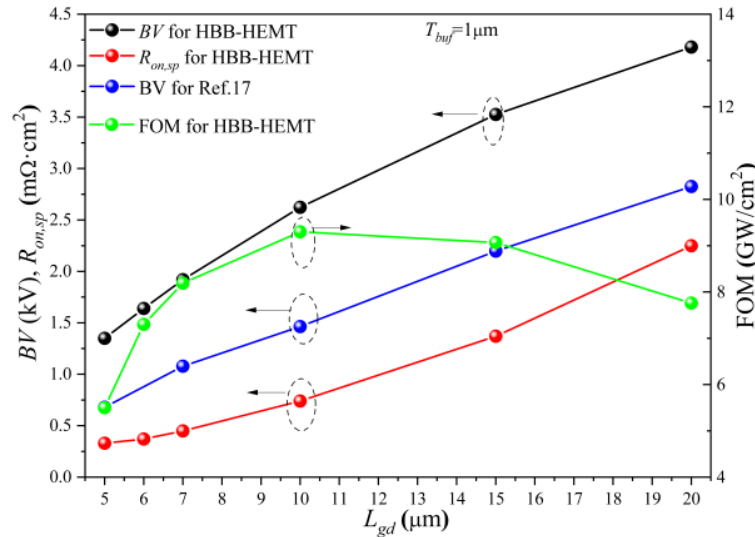

Figure 8. Breakdown voltages, $R_{on,\,sp}$, and FOM versus L_{gd} of the proposed HBB-HEMT devices.

Figure 9 presents the BV and $R_{on,\,sp}$ values of this work and the other reported devices. Due to the effective electric field modulation capability of the hybrid AlGaN back barrier, the proposed HBB-HEMT devices demonstrate significant advantages in achieving a high BV and low $R_{on,\,sp}$. The performance of other reported GaN HEMT devices is included for comparison in Figure 9 [33–39]. The proposed HBB-HEMT devices exhibit a favorable balance between BV and $R_{on,\,sp}$ relative to these previously reported results. Table 2 presents a comparison among various reported breakdown HEMTs. At L_{gd} = 10 μm, the proposed HBB-HEMT achieves a low on-resistance of 0.74 mΩ·cm^2 and a high breakdown voltage of 2623 V, yielding the best figure of merit (FOM) of 9.3 GW/cm^2 in the reported devices. Consequently, the HBB-HEMTs hold considerable promise for power electronics applications because of their high BV and low $R_{on,\,sp}$.
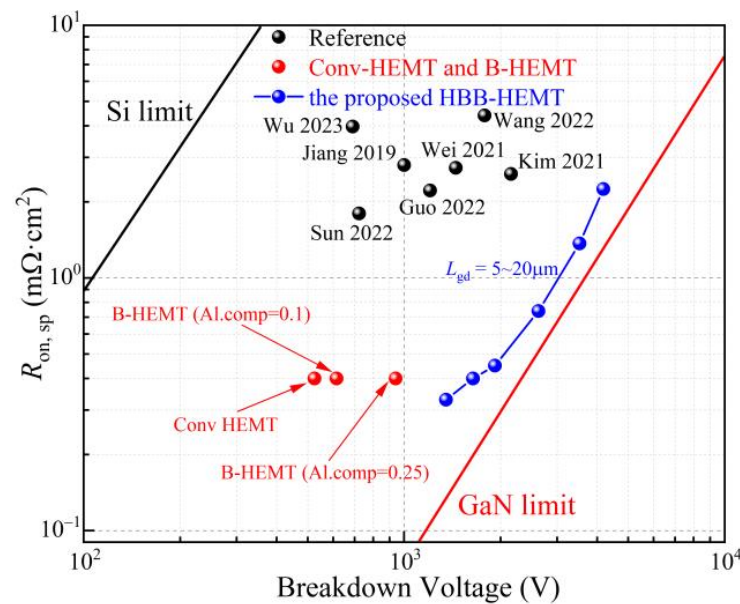

Figure 9. BV and the $R_{on,\,sp}$ for this work compared with other reported results [33–39].

Table 2. Parameters of the device in simulations.

| Year	Device	BV (V)	Ron,sp (mΩ·cm^2)	FOM (MW/cm^2)
2019	E-mode [33]	1000	2.8	357.1
2021	E-mode [34]	2154	2.58	1793.3
2021	E-mode [35]	1449	2.73	769.1
2022	E-mode [36]	723	1.80	290.4
2022	E-mode [37]	1781	4.4	720.9
2022	E-mode [38]	1205	2.22	654.1
2023	E-mode [39]	690	3.975	119
2024	This work	2623	0.74	9297.5

4.3. CV Properties

The CV characteristics of the HBB-HEMTs are shown in Figure 10. In the simulation process, we simulated the relationship between the input capacitance (C_{iss}), output capacitance (C_{oss}), reverse transfer capacitance (C_{rss}), and drain-source voltage (V_{ds}). At low drain-source voltage, the depletion region near the gate is small, resulting in a larger capacitance between the gate and drain. As the drain voltage increases, the depletion region near the gate starts to extend towards the drain, causing the channel charges between the gate and drain to be depleted. Consequently, the C_{rss} decreases with increasing drain voltage. This also applies to C_{iss} and C_{oss}, because both capacitances include C_{rss}:

$$C_{iss} = C_{gs} + C_{rss} \tag{12}$$

$$C_{oss} = C_{ds} + C_{rss} \tag{13}$$

However, for GaN HEMTs with a back barrier, due to a more uniform distribution of electric field in the channel, the depletion region extends further towards the gate, leading to a reduction in C_{rss}. From Figure 5a, it is evident that the Conv-HEMT exhibits the smallest depletion region area and thus the largest C_{rss} capacitance. The depletion region of the B-HEMT (Al.comp = 0.1) does not fully extend to the drain, resulting in a larger C_{rss} compared to the B-HEMT (Al.comp = 0.25) and HBB-HEMT. Furthermore, the presence of the back barrier enhances the confinement of the two-dimensional electron gas, thereby improving the gate's control over the channel. Therefore, GaN HEMTs with a back barrier exhibit a slight increase in C_{rss} at $V_{ds} = 0$ V. In summary, C_{rss} decreases for the HBB-HEMT at high drain voltages, which effectively improves the device's performance for high-frequency applications.
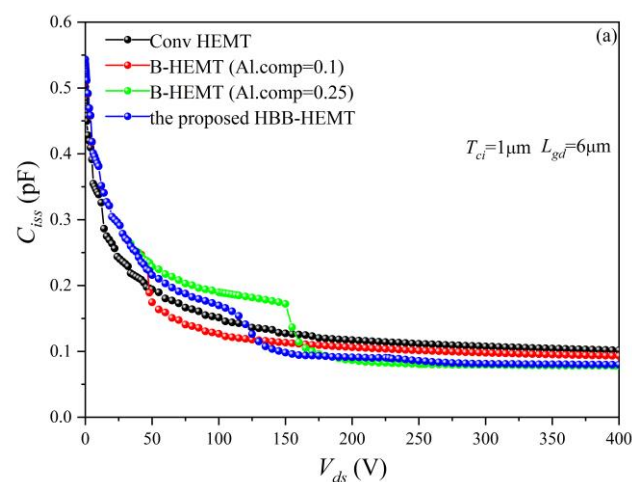
Figure 10. *Cont.*
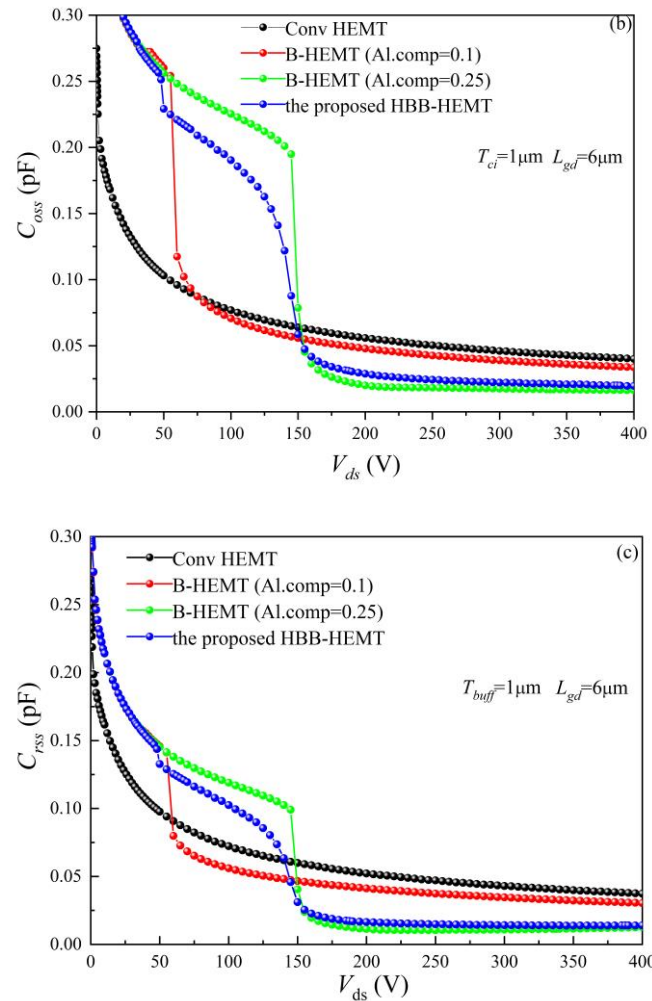
Figure 10. (**a**) Input capacitance (C_{iss}) characteristics, (**b**) output capacitance (C_{oss}) characteristics, and (**c**) reverse transfer capacitance (C_{rss}) characteristics for the HEMT devices.

4.4. Neural Network Prediction

Predicting the performance of GaN HEMTs is a complex and important task. As shown in Section 4.2, traditional prediction methods normally rely on many experiments or simulations. The BP algorithm-based neural network is a feedforward neural network. It works by updating the network's weights and biases using the backpropagation algorithm to minimize the loss function. The BP neural network has strong nonlinear modeling ability, parallel processing capability, and various optimization algorithms, making it advantageous for handling complex data from multiple physical mechanisms. To improve the efficiency of GaN HEMT performance prediction, a BP neural network model was trained in this paper and predicted the breakdown voltage of the HBB-HEMT.

4.4.1. Data Collection

For the HBB-HEMT, the distance of the gate to drain, the thickness of the GaN buffer, and the distance of the gate to the $Al_{0.25}Ga_{0.75}N/Al_{0.1}Ga_{0.9}N$ interface significantly impacted the breakdown voltage. Consequently, these three parameters were set as input variables, with the breakdown voltage as the output parameter. The value of L_{gi} is closely related to L_{gd}. Based on the optimization results from the simulations, the buffer layer thickness range was set from 0.1 to 4 μm. Since the range of L_{gi} is dependent on L_{gd}, L_{gi} was set from 0 to L_{gd}, and L_{gd} was set from 5 to 20 μm. Table 3 provides the specific values for each input parameter.

Table 3. Parameters of devices in simulations.

Parameter	Value
L_{gi}	0, 2, 3, 4,. . . . . ., L_{gd}
L_{gd}	5, 6, 7, 8, 9, 10, 11, 12, 13, 14, 15, 16, 17, 18, 19, 20
T_{buf}	0.1, 0.5, 1, 2, 3, 4

Simulations were conducted on 1296 different input parameter sets for the HBB-HEMT using TCAD Silvaco. After excluding some non-convergent results, a total of 1171 sets of breakdown voltage data with different input parameters was obtained. These simulation results were randomly divided into three groups: the training set, validation set, and test set, containing 937, 117, and 117 data points, respectively, corresponding to 80%, 10%, and 10% of the total data.

4.4.2. Establishment of Neural Network

To improve prediction accuracy, a BP neural network based on the Levenberg–Marquardt algorithm was constructed. As shown in Figure 11, the neural network architecture consisted of an input layer, a hidden layer, and an output layer. The input layer of the network had 3 neurons, representing L_{gi}, L_{gd}, and T_{buf}, respectively. The output layer had 1 neuron, representing the breakdown voltage of the HBB-HEMT. The hidden layer contained 10 neurons. During the training of the BP neural network, the maximum iterations were set to 1000, the error threshold to 0.0001, and the learning rate to 0.01.
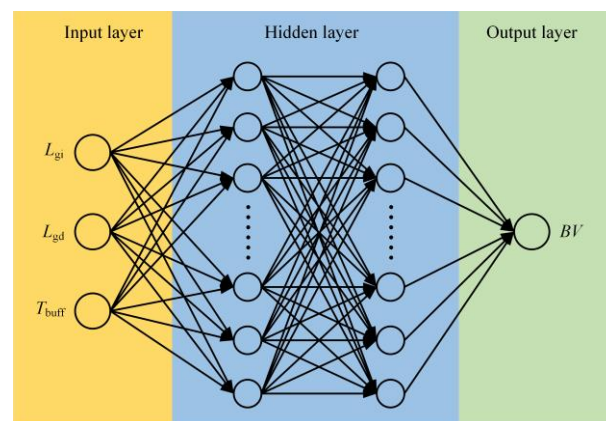
Figure 11. Structure of the BP neural network.

All simulation data were fed into the initial BP neural network model for training. Figure 12 shows the loss during the training, validation, and testing processes. When the number of iterations was greater than 7, the loss tended to be stable as the number of iterations increased. The final R coefficient values of the trained BP neural network model are shown in Figure 13. In Figure 13, the correlation coefficients R for the training set and validation set are both 0.99, which is close to 1, indicating the accuracy of the neural network model without significant overfitting. The correlation coefficient R for the test set is also 0.99, demonstrating that the trained model has sufficient generalization capability and accurate prediction ability. Figure 14 compares the predicted data from the BP neural network model with the simulation data. The average prediction error of the data comparison is 4.59%. Therefore, the BP neural network using the LM algorithm predicts the breakdown voltage of the HBB-HEMT very close to the actual values.
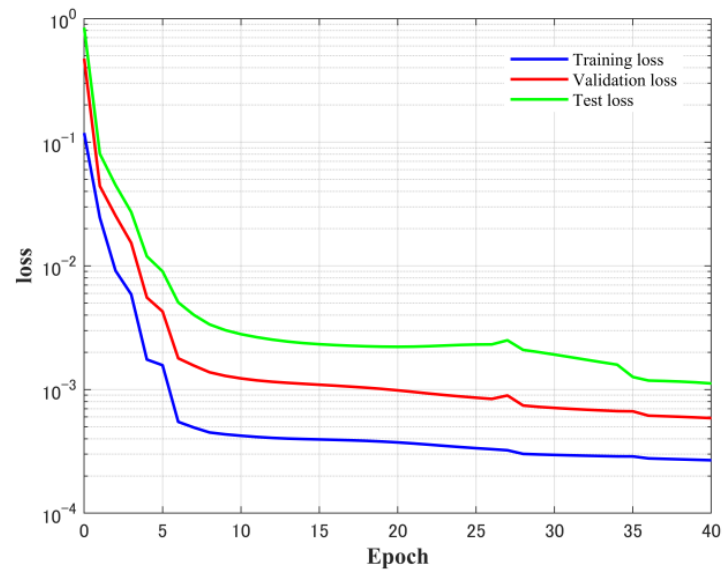
Figure 12. Loss convergence curves for training, validation, and testing.
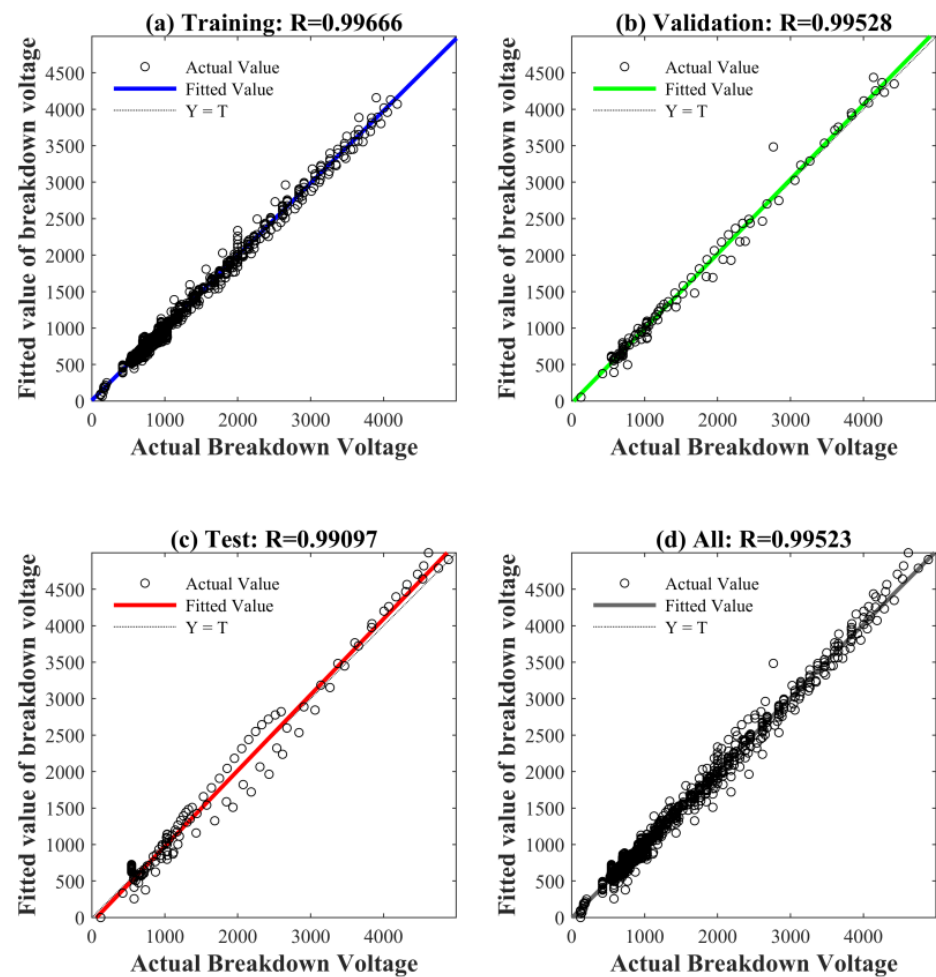

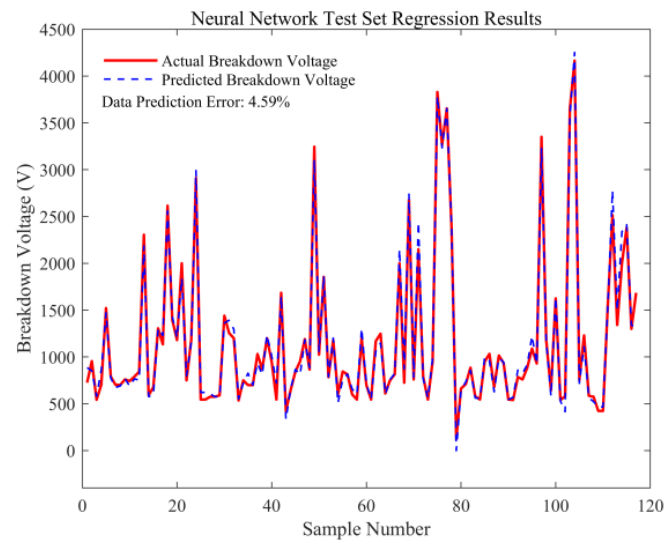**Figure 13.** Neural network training regression.

Figure 14. Comparison between BP neural network predict results and real results.

5. Conclusions

A novel HBB-HEMT was designed and optimized in this work. The hybrid AlGaN back-barrier structure could effectively modulate the electric field distributions without sacrificing forward characteristics. After proper design and optimization, the proposed HBB-HEMT achieved a high BV (1640 V), which was 212% higher than the conventional HEMT, a low $R_{on, sp}$ (0.4 mΩ·cm^2) and a high FOM (7.3 GW/cm^2). This performance was attained with an L_{gd} of 6 μm, an L_{gi} of 4.5 μm, and a T_{buf} of 1 μm. For the HBB-HEMT, the highest average breakdown electric field (2.73 MV/cm) was very close to the GaN limit, which was two times higher than that of the conventional GaN HEMT (0.88 MV/cm). Ultimately, the neural network model was used to predict the breakdown voltage of HBB-HEMTs. An average error of less than 5% indicates the accuracy of the predictive model, highlighting its significance for enhancing the efficiency of GaN HEMT design optimization.

Author Contributions: Writing—original draft, K.T.; validation, K.T.; software, K.T.; methodology, K.T.; investigation, K.T. and J.D.; conceptualization, K.T.; writing—review and editing, J.H., Q.Y. and J.D.; supervision, J.D.; resources, J.D.; formal analysis, Q.Y. All authors have read and agreed to the published version of the manuscript.

Data Availability Statement: Data are contained within the article.

Conflicts of Interest: The authors declare no conflicts of interest.

References

1. Hudgins, J.L.; Simin, G.S.; Santi, E.; Khan, M.A. An Assessment of Wide Bandgap Semiconductors for Power Devices. *IEEE Trans. Power Electron.* **2003**, *18*, 907–914. [CrossRef]
2. Dora, Y.; Chakraborty, A.; Mccarthy, L.; Keller, S.; Denbaars, S.P.; Mishra, U.K. High Breakdown Voltage Achieved on AlGaN/GaN HEMTs with Integrated Slant Field Plates. *IEEE Electron Device Lett.* **2006**, *27*, 713–715. [CrossRef]
3. Qiao, S.; Fengbo, L.; Yafang, X.; Jialin, L.; Mengxiao, L.; Xichen, Z.; Keming, Z.; Bingzhi, Z.; Yian, Y. 2.2 kV Breakdown Voltage GaN Double-Channel Schottky Barrier Diode with One Grading-AlGaN Barrier and Polarization Junction. *Micro Nanostruct.* **2023**, *178*, 207562. [CrossRef]
4. Millán, J.; Godignon, P.; Perpiñà, X.; Pérez-Tomás, A.; Rebollo, J. A Survey of Wide Bandgap Power Semiconductor Devices. *IEEE Trans. Power Electron.* **2014**, *29*, 2155–2163. [CrossRef]

5. Bhat, A.M.; Poonia, R.; Varghese, A.; Shafi, N.; Periasamy, C. AlGaN/GaN High Electron Mobility Transistor for Various Sensing Applications: A Review. *Micro Nanostruct.* **2023**, *176*, 207528. [CrossRef]

6. Bai, Y.; Xu, W.; Zhou, F.; Wang, Y.; Guo, L.; Ren, F.; Zhou, D.; Chen, D.; Zhang, R.; Zheng, Y.; et al. Over 10 kA/cm^2 Inductive Current Sustaining Capability Demonstrated in GaN-on-GaN Pn Junction with High Ruggedness. *Micro Nanostruct.* **2022**, *170*, 207367. [CrossRef]

7. Ishida, M.; Ueda, T.; Tanaka, T.; Ueda, D. GaN on Si Technologies for Power Switching Devices. *IEEE Trans. Electron Devices* **2013**, *60*, 3053–3059. [CrossRef]

8. Huang, X.; Liu, Z.; Lee, F.C.; Li, Q. Characterization and Enhancement of High-Voltage Cascode GaN Devices. *IEEE Trans. Electron Devices* **2015**, *62*, 270–277. [CrossRef]

9. Zhong, K.; Wang, Y.; Lyu, G.; Wei, J.; Sun, J.; Chen, K.J. 650-V Normally-OFF GaN/SiC Cascode Device for Power Switching Applications. *IEEE Trans. Ind. Electron.* **2022**, *69*, 8997–9006. [CrossRef]

10. Oka, T.; Nozawa, T. AlGaN/GaN Recessed MIS-Gate HFET with High-Threshold-Voltage Normally-off Operation for Power Electronics Applications. *IEEE Electron Device Lett.* **2008**, *29*, 668–670. [CrossRef]

11. Hua, M.; Zhang, Z.; Wei, J.; Lei, J.; Tang, G.; Fu, K.; Cai, Y.; Zhang, B.; Chen, K.J. Integration of LPCVD-SiNx Gate Dielectric with Recessed-Gate E-Mode GaN MIS-FETs: Toward High Performance, High Stability and Long TDDB Lifetime. In Proceedings of the 2016 IEEE International Electron Devices Meeting (IEDM), San Francisco, CA, USA, 3–7 December 2016; pp. 10.4.1–10.4.4. [CrossRef]

12. Zhang, Z.; Fu, K.; Deng, X.; Zhang, X.; Fan, Y.; Sun, S.; Song, L.; Xing, Z.; Huang, W.; Yu, G.; et al. Normally Off AlGaN/GaN MIS-High-Electron Mobility Transistors Fabricated by Using Low Pressure Chemical Vapor Deposition Si$_3$N$_4$ Gate Dielectric and Standard Fluorine Ion Implantation. *IEEE Electron Device Lett.* **2015**, *36*, 1128–1131. [CrossRef]

13. Han, P.-C.; Yan, Z.-Z.; Wu, C.-H.; Chang, E.Y.; Ho, Y.-H. Recess-Free Normally-off GaN MIS-HEMT Fabricated on Ultra-Thin-Barrier AlGaN/GaN Heterostructure. In Proceedings of the 2019 31st International Symposium on Power Semiconductor Devices and ICs (ISPSD), Shanghai, China, 19–23 May 2019; pp. 427–430. [CrossRef]

14. Hilt, O.; Brunner, F.; Cho, E.; Knauer, A.; Bahat-Treidel, E.; Würfl, J. Normally-off High-Voltage p-GaN Gate GaN HFET with Carbon-Doped Buffer. In Proceedings of the 2011 IEEE 23rd International Symposium on Power Semiconductor Devices and ICs, San Diego, CA, USA, 23–26 May 2011; pp. 239–242. [CrossRef]

15. Ge, M.; Li, Y.; Zhu, Y.; Chen, D.; Wang, Z.; Tan, S. Suppression of Leakage Current of P-GaN Gate AlGaN/GaN HEMTs with Beta-Ga2O3 Back Barrier. *J. Phys. D Appl. Phys.* **2021**, *55*, 065104. [CrossRef]

16. Jia, M.; Hou, B.; Yang, L.; Zhang, M.; Chang, Q.; Niu, X.; Shi, C.; Du, J.; Wu, M.; Lu, H.; et al. Simulation and Analysis of Enhancement-Mode AlGaN/GaN HEMT with P-I-N Junction Gate. *J. Phys. D Appl. Phys.* **2024**, *57*, 265101. [CrossRef]

17. Handa, H.; Ujita, S.; Shibata, D.; Kajitani, R.; Shiozaki, N.; Ogawa, M.; Umeda, H.; Tanaka, K.; Tamura, S.; Hatsuda, T.; et al. High-Speed Switching and Current-Collapse-Free Operation by GaN Gate Injection Transistors with Thick GaN Buffer on Bulk GaN Substrates. In Proceedings of the 2016 IEEE International Electron Devices Meeting (IEDM), San Francisco, CA, USA, 3–7 December 2016; pp. 10.3.1–10.3.4. [CrossRef]

18. Tanaka, K.; Morita, T.; Umeda, H.; Kaneko, S.; Kuroda, M.; Ikoshi, A.; Yamagiwa, H.; Okita, H.; Hikita, M.; Yanagihara, M.; et al. Suppression of Current Collapse by Hole Injection from Drain in a Normally-off GaN-Based Hybrid-Drain-Embedded Gate Injection Transistor. *Appl. Phys. Lett.* **2015**, *107*, 163502. [CrossRef]

19. Aamir Ahsan, S.; Ghosh, S.; Sharma, K.; Dasgupta, A.; Khandelwal, S.; Chauhan, Y.S. Capacitance Modeling in Dual Field-Plate Power GaN HEMT for Accurate Switching Behavior. *IEEE Trans. Electron Devices* **2016**, *63*, 565–572. [CrossRef]

20. Lee, H.-S.; Piedra, D.; Sun, M.; Gao, X.; Guo, S.; Palacios, T. 3000-V 4.3-mΩ·cm^2 InAlN/GaN MOSHEMTs with AlGaN Back Barrier. *IEEE Electron Device Lett.* **2012**, *33*, 982–984. [CrossRef]

21. Kilic, A.; Yildirim, R.; Eroglu, D. Machine Learning Analysis of Ni/SiC Electrodeposition Using Association Rule Mining and Artificial Neural Network. *J. Electrochem. Soc.* **2021**, *168*, 62514. [CrossRef]

22. Hari, N.; Ahsan, M.; Ramasamy, S.; Sanjeevikumar, P.; Albarbar, A.; Blaabjerg, F. Gallium Nitride Power Electronic Devices Modeling Using Machine Learning. *IEEE Access* **2020**, *8*, 119654–119667. [CrossRef]

23. Ma, H.; Duan, X.; Wang, S.; Liu, S.; Zhang, J.; Hao, Y. GaN JBS Diode Device Performance Prediction Method Based on Neural Network. *Micromachines* **2023**, *14*, 188. [CrossRef]

24. Jiang, Z.; Jiang, Y.; Chen, M.; Li, J.; Li, P.; Chen, B.; Zhao, S.; Wang, J.; Jiang, S.; Cai, M.; et al. Advanced Design of a III-Nitride Light-Emitting Diode via Machine Learning. *Laser Photonics Rev.* **2023**, *17*, 2300113. [CrossRef]

25. Bernardini, F.; Fiorentini, V.; Vanderbilt, D. Spontaneous Polarization and Piezoelectric Constants of III-V Nitrides. *Phys. Rev. B* **1997**, *56*, R10024–R10027. [CrossRef]

26. Ambacher, O.; Majewski, J.; Miskys, C.; Link, A.; Hermann, M.; Eickhoff, M.; Stutzmann, M.; Bernardini, F.; Fiorentini, V.; Tilak, V.; et al. Pyroelectric Properties of Al(In)GaN/GaN Hetero- and Quantum Well Structures. *J. Phys. Condens. Matter* **2002**, *14*, 3399. [CrossRef]

27. Ambacher, O.; Smart, J.; Shealy, J.R.; Weimann, N.G.; Chu, K.; Murphy, M.; Schaff, W.J.; Eastman, L.F.; Dimitrov, R.; Wittmer, L.; et al. Two-Dimensional Electron Gases Induced by Spontaneous and Piezoelectric Polarization Charges in N- and Ga-Face AlGaN/GaN Heterostructures. *J. Appl. Phys.* **1999**, *85*, 3222–3233. [CrossRef]

28. Albrecht, J.D.; Wang, R.P.; Ruden, P.P.; Farahmand, M.; Brennan, K.F. Electron Transport Characteristics of GaN for High Temperature Device Modeling. *J. Appl. Phys.* **1998**, *83*, 4777–4781. [CrossRef]

29. Farahmand, M.; Garetto, C.; Bellotti, E.; Brennan, K.F.; Goano, M.; Ghillino, E.; Ghione, G.; Albrecht, J.D.; Ruden, P.P. Monte Carlo simulation of electron transport in the III-nitride wurtzite phase materials system: Binaries and ternaries. *IEEE Trans. Electron Devices* **2001**, *48*, 535–542. [CrossRef]

30. Bulutay, C. Electron Initiated Impact Ionization in AlGaN Alloys. *Semicond. Sci. Technol.* **2002**, *17*, L59. [CrossRef]

31. Bai, Z.; Du, J.; Liu, Y.; Xin, Q.; Liu, Y.; Yu, Q. Study on the Electrical Degradation of AlGaN/GaN MIS-HEMTs Induced by Residual Stress of SiNx Passivation. *Solid-State Electron.* **2017**, *133*, 31–37. [CrossRef]

32. Visalli, D.; Van Hove, M.; Srivastava, P.; Derluyn, J.; Das, J.; Leys, M.; Degroote, S.; Cheng, K.; Germain, M.; Borghs, G. Experimental and Simulation Study of Breakdown Voltage Enhancement of AlGaN/GaN Heterostructures by Si Substrate Removal. *Appl. Phys. Lett.* **2010**, *97*, 113501. [CrossRef]

33. Jiang, H.; Zhu, R.; Lyu, Q.; Lau, K.M. High-Voltage p-GaN HEMTs with OFF-State Blocking Capability After Gate Breakdown. *IEEE Electron Device Lett.* **2019**, *40*, 530–533. [CrossRef]

34. Kim, J.-G.; Cho, C.; Kim, E.; Hwang, J.S.; Park, K.-H.; Lee, J.-H. High breakdown voltage and low-current dispersion in AlGaN/GaN HEMTs with high-quality AlN buffer layer. *IEEE Trans. Electron Devices* **2021**, *68*, 1513–1517. [CrossRef]

35. Wei, X.; Zhang, X.; Sun, C.; Tang, W.; Zeng, C.; Chen, F.; He, T.; Yu, G.; Song, L.; Lin, W.; et al. Improvement of breakdown voltage and ON-resistance in normally-OFF AlGaN/GaN HEMTs using etching-free p-GaN stripe array gate. *IEEE Trans. Electron Devices* **2021**, *68*, 5041–5047. [CrossRef]

36. Sun, T.; Yang, K.; Wei, J.; Jia, Y.; Deng, S.; Zhao, Z.; Zhang, B.; Luo, X. High-voltage polarization-superjunction GaN HEMT with built-In SBD for low reverse conduction loss. *IEEE J. Electron Devices Soc.* **2022**, *10*, 808–812. [CrossRef]

37. Wang, Y.; Hu, S.; Guo, J.; Wu, H.; Liu, T.; Jiang, J. Enhancement of breakdown voltage in p-GaN gate AlGaN/GaN HEMTs with a stepped hybrid GaN/AlN buffer layer. *IEEE J. Electron Devices Soc.* **2022**, *10*, 197–202. [CrossRef]

38. Guo, H.; Gong, H.; Shao, P.; Yu, X.; Wang, J.; Wang, R.; Yu, L.; Ye, J.; Chen, D.; Lu, H.; et al. Over 1200 V normally-OFF p-NiO gated AlGaN/GaN HEMTs on Si with a small threshold voltage shift. *IEEE Electron Device Lett.* **2022**, *43*, 268–271. [CrossRef]

39. Wu, N.; Luo, L.; Xing, Z.; Li, S.; Zeng, F.; Cao, B.; Wu, C.; Li, G. Enhanced performance of low-leakage-current normally off p-GaN gate HEMTs using NH3 plasma pretreatment. *IEEE Trans. Electron Devices* **2023**, *70*, 4560–4564. [CrossRef]